Patient-specific computational modeling of subendothelial LDL accumulation in a stenosed right coronary artery: effect of hemodynamic and biological factors

Antonis I. Sakellarios, Michail I. Papafaklis, Panagiotis Siogkas, Lambros S. Athanasiou, Themistoklis P. Exarchos, Konstantinos Stefanou, Christos V. Bourantas, Katerina K. Naka, Lampros K. Michalis, Oberdan Parodi and Dimitrios I. Fotiadis

Am J Physiol Heart Circ Physiol 304:H1455-H1470, 2013. First published 15 March 2013;
doi: 10.1152/ajpheart.00539.2012

Am J Physiol Heart Circ Physiol 304: H1455–H1470, 2013.
First published March 15, 2013; doi:10.1152/ajpheart.00539.2012.

Patient-specific computational modeling of subendothelial LDL accumulation in a stenosed right coronary artery: effect of hemodynamic and biological factors

Antonis I. Sakellarios,[1] Michail I. Papafaklis,[2] Panagiotis Siogkas,[1] Lambros S. Athanasiou,[1] Themistoklis P. Exarchos,[3] Konstantinos Stefanou,[3] Christos V. Bourantas,[4] Katerina K. Naka,[5,6] Lampros K. Michalis,[5,6] Oberdan Parodi,[7] and Dimitrios I. Fotiadis[1,3,5]

[1]*Unit of Medical Technology and Intelligent Information Systems, Department of Materials Science and Engineering, University of Ioannina, Ioannina, Greece;* [2]*Cardiovascular Division, Brigham and Women's Hospital, Harvard Medical School, Boston, Massachusetts;* [3]*Biomedical Research Institute-FORTH, University Campus of Ioannina, Ioannina, Greece;* [4]*Department of Interventional Cardiology, Erasmus MC, Thoraxcenter, Rotterdam, The Netherlands;* [5]*Michailideion Cardiac Center, University of Ioannina, Ioannina, Greece;* [6]*Department of Cardiology, Medical School, University of Ioannina, Ioannina, Greece; and* [7]*Instituto di Fisiologia Clinica, Consiglio Nazionale delle Ricerche, Pisa, Italy*

Submitted 16 July 2012; accepted in final form 5 March 2013

Sakellarios AI, Papafaklis MI, Siogkas P, Athanasiou LS, Exarchos TP, Stefanou K, Bourantas CV, Naka KK, Michalis LK, Parodi O, Fotiadis DI. Patient-specific computational modeling of subendothelial LDL accumulation in a stenosed right coronary artery: effect of hemodynamic and biological factors. *Am J Physiol Heart Circ Physiol* 304: H1455–H1470, 2013. First published March 15, 2013; doi:10.1152/ajpheart.00539.2012.—Atherosclerosis is a systemic disease with local manifestations. Low-density lipoprotein (LDL) accumulation in the subendothelial layer is one of the hallmarks of atherosclerosis onset and ignites plaque development and progression. Blood flow-induced endothelial shear stress (ESS) is causally related to the heterogenic distribution of atherosclerotic lesions and critically affects LDL deposition in the vessel wall. In this work we modeled blood flow and LDL transport in the coronary arterial wall and investigated the influence of several hemodynamic and biological factors that may regulate LDL accumulation. We used a three-dimensional model of a stenosed right coronary artery reconstructed from angiographic and intravascular ultrasound patient data. We also reconstructed a second model after restoring the patency of the stenosed lumen to its nondiseased state to assess the effect of the stenosis on LDL accumulation. Furthermore, we implemented a new model for LDL penetration across the endothelial membrane, assuming that endothelial permeability depends on the local lumen LDL concentration. The results showed that the presence of the stenosis had a dramatic effect on the local ESS distribution and LDL accumulation along the artery, and areas of increased LDL accumulation were observed in the downstream region where flow recirculation and low ESS were present. Of the studied factors influencing LDL accumulation, *1*) hypertension, *2*) increased endothelial permeability (a surrogate of endothelial dysfunction), and *3*) increased serum LDL levels, especially when the new model of variable endothelial permeability was applied, had the largest effects, thereby supporting their role as major cardiovascular risk factors.

low-density lipoprotein transport; shear stress; atherosclerosis; endothelial permeability; risk factors; patient-specific simulations

CORONARY ARTERY DISEASE (CAD) is an epidemic in Western societies and is projected to be the most common cause of morbidity and mortality worldwide in the following decades (54a). Atherosclerosis is initiated by the accumulation of plasma-derived lipoproteins in the arterial wall, launching specific pathophysiological pathways. Abnormal accumulations of lipoproteins and cholesterol esters and increased concentrations of inflammatory cells, mainly macrophages, are detected in the intima of initial lesions. The histological identification of small, isolated groups of macrophages containing lipid droplets (macrophage foam cells) is the hallmark of atherosclerosis and characterizes fatty streaks (type I lesions; American Heart Association classification) (40, 41).

Despite the effect of systemic risk factors, atherosclerosis is a site-specific disease. The localization of early lesions depends on hemodynamic forces, endothelial shear stress (ESS) in particular, which act on the vessel wall (24). In a purely mechanistic viewpoint, low ESS increases the residence time between blood particles [e.g., low-density lipoprotein (LDL)] and the arterial wall and consequently increases the transendothelial diffusion and influx. This is in accordance with the higher propensity of atherosclerotic lesions to develop at specific locations in the vasculature, including the lateral walls of arterial bifurcations and the inner side of curved arterial segments, where blood flow is slow and ESS is predominantly low, thereby activating proatherogenic pathways in endothelial cells. Furthermore, changes in local arterial geometry induced by a growing, obstructive plaque have a great impact on the spatial distribution of local ESS. The regional plaque-induced changes of local ESS, in turn, may critically affect the longitudinal distribution of plaque morphology, promoting a self-perpetuating local hemodynamic environment conducive to lipid accumulation and further plaque growth (6, 19).

The latest advances in mathematical and computational modeling have enabled the detailed investigation of hemodynamic factors in atherosclerosis, providing invaluable knowledge of the detailed spatiotemporal variations that shear stress may exhibit while the parameters that determine each set of hemodynamic conditions are completely controlled. Although ESS computation is critical in identifying regions prone to atherosclerosis, LDL transport and accumulation in the arterial wall directly reflect a critical part of the pathophysiological process (28). Therefore, computational modeling of LDL trans-

Address for reprint requests and other correspondence: D. I. Fotiadis, Unit of Medical Technology and Intelligent Information Systems, Dept. of Materials Science and Engineering, Univ. of Ioannina, PO Box 1186, GR 451 10 Ioannina, Greece (e-mail: fotiadis@cc.uoi.gr).

port has been lately proposed, and several models (e.g., wall-free, lumen-wall and multilayer models) have been developed that provide different levels of description of the arterial wall, simulating the complexities of the in vivo condition to a variable extent (29, 35).

Initial computational studies focusing mainly on the influence of ESS on plaque development/progression mostly used idealized simplified arterial geometries (48). Realistic three-dimensional (3D) arterial models of the aorta, the carotids, and, less frequently, the coronary arteries (26, 32, 33, 42), have also been employed. Lately, data on 3D modeling of LDL mass transport have become available; early studies in either theoretical models of stenosed arteries or anatomically correct coronary lumen models employed LDL mass transport within the lumen and highlighted the role of hemodynamic ESS in LDL transfer rates, while they emphasized the importance of accurate geometrical reconstruction of arteries when assessing LDL mass concentration (16, 17). There have been few studies investigating the fluid-wall coupled mass transport (i.e., mass transport in both the lumen and the arterial wall) in patient-specific geometries of atherosclerotic coronary arteries (28, 30, 45).

In addition, the application of specific boundary conditions on both the flow field (e.g., steady-state vs. transient flow) and the mass transport modeling [e.g., ESS-dependent hydraulic conductivity (45, 48)] is critical in determining the computational solution and the realistic simulation of specific conditions in a given patient. The development of atherosclerotic lesions is a multifactorial process dependent on a variety of biological (risk factors: hyperlipidemia, hypertension, and diabetes) and hemodynamic factors altering the function of the endothelial layer and thus triggering plaque formation. Therefore, a customized approach may be necessary to better reflect the localized deposition of LDL on the endothelial surface and the overall burden of LDL accumulation in the arterial wall, taking into account the specific cardiovascular risk profile of an individual.

In the current report, we compute the subendothelial LDL accumulation in a 3D patient-specific model of an atherosclerotic coronary artery, investigating the plaque-induced effects of a stenotic region on the ESS and LDL distribution. Coronary artery reconstruction was obtained from the fusion of angiographic and intravascular ultrasound (IVUS) data, which provide high-resolution information about the lumen and the arterial wall. To evaluate the effects of the stenosis on ESS distribution and LDL accumulation, we also performed an additional artery reconstruction after artificially restoring the lumen patency to its nondiseased state. Furthermore, we quantify for the first time the influence exerted on computed LDL accumulation by *1*) hemodynamic parameters, which are considered to be important in blood flow modeling, and, more importantly, *2*) biological factors (e.g., LDL serum level, hypertension, endothelial dysfunction) that determine the specific cardiovascular risk profile of a patient. Finally, we implement a novel model of endothelial permeability with locally varying values that depend on the regional lumen LDL concentration based on literature experimental data.

Glossary

c_{adv}	Adventitial LDL concentration (mol/m^3)
c_0	Inlet LDL concentration (mol/m^3)
c_l	Luminal LDL concentration (mol/m^3)
c_w	LDL concentration in the arterial wall (mol/m^3)
D_l	Luminal LDL diffusivity (m^2/s)
D_w	LDL diffusivity in the artery wall (m^2/s)
J_v	Transmural velocity (m/s)
J_s	Solute flux (mol·s^{-1}·m^{-2})
K_{lag}	Solute lag coefficient
L_p	Hydraulic conductivity (m·s^{-1}·Pa^{-1})
P_0	Diffusive endothelial permeability (m/s)
P_e	Apparent (overall) endothelial permeability (m/s)
p	Pressure (mmHg)
p_w	Pressure in the arterial wall (mmHg)
r_w	Consumption rate constant (s^{-1})
$\mathbf{u}_l$	Blood velocity in the lumen (m/s)
$\mathbf{u}_w$	Transmural velocity in the arterial wall (m/s)
Δp	Pressure difference (mmHg)
$\Delta\pi$	Oncotic pressure difference (mmHg)
κ_w	Darcian permeability coefficient (m^2)
μ	Blood viscosity (Pa·s)
μ_p	Dynamic viscosity of the plasma (Pa·s)
ρ	Blood density (kg/m^3)
σ_d, σ_f	Reflection coefficients
τ_w	Endothelial shear stress (Pa)

METHODS

Patient data and 3D coronary artery reconstruction. A 66-year-old male patient with a history of diabetes, hypercholesterolemia, and hypertension underwent coronary angiography because of angina symptoms. Coronary angiography (Fig. 1*A*) revealed a moderately significant stenosis in the mid right coronary artery (RCA). IVUS examination was performed for clinical purposes to thoroughly assess the stenotic region and plan interventional treatment, and showed a large eccentric plaque [plaque burden (plaque area/vessel area): 83% and minimum lumen area: 3.7 mm^2; Fig. 1*B*]. Written informed consent was obtained from the patient for use of the data for research purposes.

Coronary artery reconstruction was performed using a validated methodology based on the fusion of angiographic and IVUS data as previously described (2). Briefly, the IVUS catheter (Atlantis SR 40 MHz; Boston Scientific, Natick, MA) was advanced to the distal RCA, and angiographic images from two orthogonal views were acquired after contrast agent injection. The IVUS catheter was then withdrawn at a constant speed (0.5 mm/s) using an automated pull-back device. The obtained data were digitized and transferred to a workstation for further processing. The lumen and media-adventitia borders were detected in the end-diastolic images of the IVUS sequence and placed perpendicularly onto the 3D catheter path extracted from two end-diastolic angiographic images. The orientation of the IVUS frames onto the path was then determined using efficient algorithms. The outcome of this process was two point clouds that represented the luminal and media-adventitia wall geometry.

An additional reconstruction of the lumen of the RCA was performed that represented the geometry of the lumen after its patency was restored. At the site of the stenosis, the IVUS lumen borders of the model with restored patency were approximated by the segmentation of the arterial lumen including the detected plaque; the border of the restored lumen was delineated parallel to the outer vessel wall border and kept at a constant distance around the circumference. To partially take into account any outward wall remodeling process and more accurately represent the restored lumen, the size of the restored lumen area at each axial location (i.e., IVUS cross section) along the length of the stenosed region was calculated by linear interpolation between the lumen areas of the proximal and distal reference regions. These data were used to reconstruct the lumen and obtain a 3D model that corresponded to the "nondiseased" RCA model. The three point

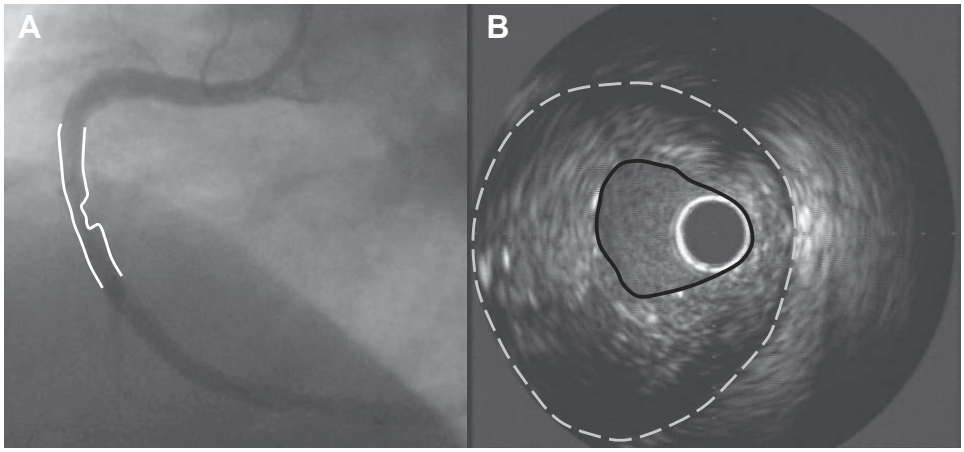

Fig. 1. *A*: left anterior oblique angiographic view of the right coronary artery demonstrating a moderately significant stenosis in the midsection. The lumen borders in this region are indicated in white. *B*: intravascular ultrasound cross-sectional image demonstrating an eccentric lesion with a minimum lumen area of 3.7 mm^2. The borders of the lumen (black solid line) and the outer vessel wall (white dotted line) are denoted.

clouds, representing the stenosed RCA lumen, the vessel wall, and the nondiseased RCA lumen, were processed to non-uniform rational B-spline (NURBS) surfaces (Fig. 2).

Blood flow modeling. Blood flow was modeled using the incompressible Navier-Stokes and continuity equations:

$$\rho\frac{\partial \mathbf{u}_l}{\partial t} - \mu\nabla^2\mathbf{u}_l + \rho(\mathbf{u}_l \cdot \nabla)\mathbf{u}_l + \nabla p = 0, \quad (1)$$

$$\nabla \cdot \mathbf{u}_l = 0, \quad (2)$$

where $\mathbf{u}_l$ is the blood velocity in the lumen, p is the pressure, and ρ (1,060 kg/m^3) and μ are the blood density and viscosity, respectively. Blood was assumed to behave as a Newtonian fluid (μ = 0.0035 Pa·s), since it has been previously shown that the non-Newtonian blood properties have a minimal effect on LDL accumulation (22).

Blood flow was considered to be laminar, and a no-slip boundary condition was applied at the wall, which was assumed to be rigid. The patient-specific blood flow (1.5 ml/s; uniform velocity profile) at the inlet was calculated directly from the time required for the volume of blood contained within the 3D reconstructed arterial segment to be displaced by radio-opaque material during an angiographic contrast injection (44). Two inlet velocity boundary conditions were implemented: steady-state and pulsatile flow; an RCA-specific pulsatile flow waveform (Fig. 3) based on literature data (13) was used after the values were adjusted so that the time-averaged flow would be equal to the patient-specific steady-state flow (1.5 ml/s). Furthermore, we used two pulsatile profiles: one with a normal heart rate (normal profile: 80 beats/min) and one with a heart rate raised by 50% (tachycardia profile: 120 beats/min; Fig. 3); the ratio of diastolic to systolic duration was set at 2:1 for the normal heart rate and 1:1 for the tachycardia. Three cardiac cycles were utilized for each transient simulation, where the time step was 1/100 of the cardiac cycle, thus providing time independence of the simulation. The results of the third cycle were used for the analysis. At the outlet of the lumen, pressure

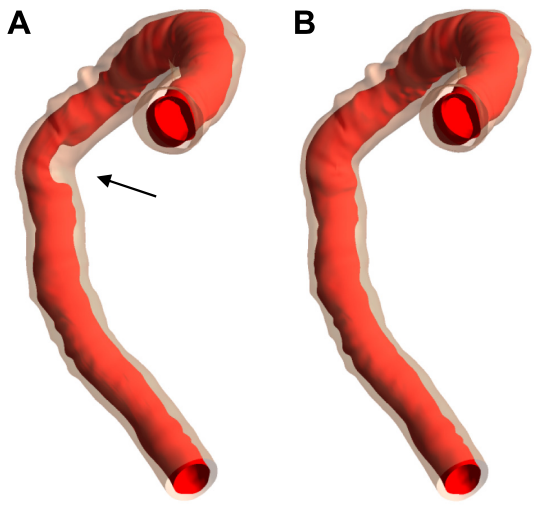

Fig. 2. Three-dimensional lumen (red) and vessel wall (beige) reconstructed geometry of the right coronary artery for the stenosed model (*A*) based on the original imaging data, including the region of stenosis (arrow) in the midsection, and the "nondiseased" model (*B*) after artificially restoration of the patency of the lumen.

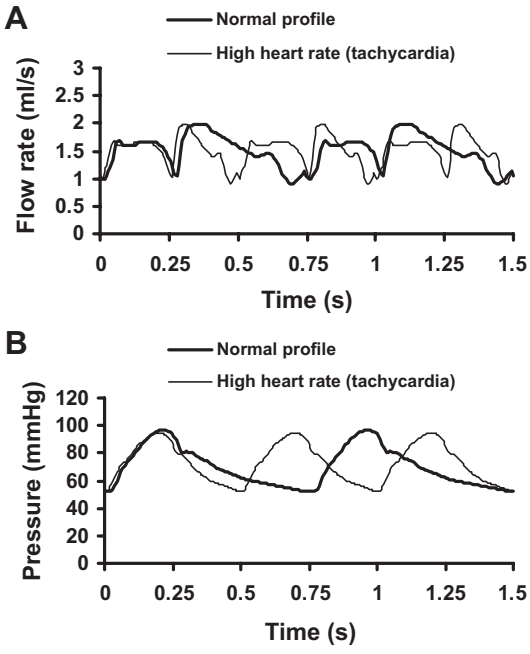

Fig. 3. *A*: pulsatile flow profile applied at the inlet of the artery for the transient flow simulations: normal heart rate (80 beats/min; thick line) and tachycardia (120 beats/min; thin line). The values of both flow profiles have been adjusted so that the time-averaged flow rate during one cardiac cycle equals 1.5 ml/s, which is the patient-specific flow rate used in the steady flow simulations. *B*: pulsatile pressure waveform applied at the outlet of the artery for the transient flow simulations with time-averaged value equal to the one (70 mmHg) used for the steady-state simulation; the respective profiles for the normal heart rate (thick line) and tachycardia (thin line) are provided. The ratio of diastolic to systolic duration was set to 2:1 and 1:1 in the normal heart rate and tachycardia, respectively.

values of 70 and 120 mmHg were applied to simulate the normal and hypertensive conditions (30), respectively; in the case of pulsatile flow, the pressure waveform presented in Fig. 3 with a time-averaged pressure equal to the one for the normal condition (70 mmHg) of the steady-state simulation was used.

Plasma filtration in the arterial wall. The arterial wall was assumed to be a porous media. Thus the plasma filtration was modeled using Darcy's law:

$$\mathbf{u}_w - \nabla \cdot \left(\frac{\kappa_w}{\mu_p} p_w \right) = 0, \quad (3)$$

$$\nabla \cdot \mathbf{u}_w = 0, \quad (4)$$

where $\mathbf{u}_w$ is the transmural velocity of the plasma in the arterial wall, p_w is the arterial wall pressure, μ_p is the dynamic viscosity of the plasma, and κ_w is the Darcian permeability coefficient in the arterial wall.

No flux of plasma was assumed at the two longitudinal ends of the arterial wall. At the media-adventitia border, a boundary pressure of 17.5 or 30 mmHg (30) was applied for the normal or hypertensive condition, respectively.

Mass transport modeling. Blood was considered to be a homogenous dilution with LDL, and LDL particle size was assumed not to influence the blood flow. The convection-diffusion equation was used to approximate the LDL transport in the lumen:

$$\nabla \cdot \left(-D_l \nabla c_l + c_l \mathbf{u}_l \right) = 0, \quad (5)$$

where C_l is the luminal LDL concentration and D_l is the luminal LDL diffusivity.

LDL transport in the vessel wall was described using the convection-diffusion equation, with the addition of a term for the degradation of LDL due to oxidation:

$$\nabla \cdot \left(-D_w \nabla c_w + K_{lag} c_w \mathbf{u}_w \right) = r_w c_w, \quad (6)$$

where c_w is the LDL concentration in the arterial wall, D_w is the diffusivity of the solute in the arterial wall, K_{lag} is the solute lag coefficient for the LDL, and r_w is the consumption rate constant.

Four different clinically meaningful LDL concentration values were investigated as inlet boundary conditions: since the cholesterol in LDL (LDL-cholesterol concentration) has been the standard measure for attributing the risk for cardiovascular disease in clinical practice, we first defined the four different values of clinical interest according to LDL-cholesterol: 1.8 mol/m^3 (70 mg/dl), ideal target value for patients at very high cardiovascular risk; 2.6 mol/m^3 (100 mg/dl), target value for patients at high risk; 4.1 mol/m^3 (160 mg/dl), normal upper limit in the general population; and 5.2 mol/m^3 (200 mg/dl), which represents an increased value above the normal limit. We then incorporated the LDL-cholesterol values into our computational studies by translating them into the respective LDL (i.e., LDL particles) concentrations using the average conversion of 100 mg/dl LDL-cholesterol to 1.06×10^{-3} mol/m^3 LDL based on latest human data (31). The corresponding LDL particle concentrations were as follows: 0.742, 1.06, 1.696, and 2.12×10^{-3} mol/m^3. A constant LDL concentration value of $C_{adv} = 0.005 \cdot C_0$ or $C_{adv} = 0.015 \cdot C_0$ was applied at the media-adventitia boundary for the normal or hypertensive case (30), respectively.

Modeling of endothelial permeability. The LDL flux across the endothelial membrane was modeled using the Kedem-Katchalsky equations (18):

$$J_v = L_p(\Delta p - \sigma_d \Delta \pi), \quad (7)$$

$$J_s = P_0 \Delta c + (1 - \sigma_f) J v \bar{c}, \quad (8)$$

where J_v is the transmural velocity and J_s is the solute flux through the endothelium, L_p is the hydraulic conductivity, Δp and $\Delta \pi$ are the pressure difference and the oncotic pressure difference across the endothelial membranes, respectively, P_0 is the diffusive endothelial permeability, c is the solute concentration, $\bar{c}$ is the mean endothelial concentration, and σ_d, σ_f are the reflection coefficients. We modeled a normal value of overall (apparent) permeability ($P_e = 2 \times 10^{-10}$ m/s) (39, 52), as well as a double overall permeability value ($P_e = 4 \times 10^{-10}$ m/s) mimicking diseased states with endothelial dysfunction such as in diabetes mellitus or hypertension (36, 50). Diffusive permeability values in *Eq. 8* ($P_0 = 1.5 \times 10^{-10}$ m/s and $P_0 = 3.53 \times 10^{-10}$ m/s for the normal and double overall permeability conditions, respectively) were derived from the previously reported system of equations describing solute transport via diffusion and convection through a single pathway (34, 49), as described in the APPENDIX. In the current study, the oncotic pressure difference was neglected to decouple the fluid dynamics from solute dynamics as it has been previously implemented (29, 45).

Furthermore, on the basis of previous experimental and computational studies (37, 45, 47), it was considered that the hydraulic conductivity depends on ESS with the use of the following equation:

$$L_p(|\tau_w|) = 0.3881 \times 10^{-12} \ln(|\tau_w| + 0.015) + 2.7656 \times 10^{-12}, \quad (9)$$

where $|\tau_w|$ is the absolute value of ESS. The numerical coefficients were specifically calculated for the computational geometry in our study by using the normalized data from Sill et al. (37), the average ESS value at the inlet of the upstream region of the stenosis, and an assumed reference value of constant hydraulic conductivity equal to $L_p = 3 \times 10^{-12}$ m·s^{-1}·Pa^{-1} (47). In the case of pulsatile flow, ESS values were first computed at each time step and were used for the calculation of hydraulic conductivity at the same time step. Thus a time-dependent value of hydraulic conductivity was implemented and used for the unsteady mass transport computations.

The relationship between ESS and L_p dictates that the endothelium demonstrates increased permeability to blood macromolecules when subject to higher ESS. The hemodynamic stimulus on endothelial cells is mediated by mechanoreceptors linked to critical signaling pathways (e.g., NO-dependent mechanisms) and involves the conversion of the biomechanical stimuli to biochemical responses. In this context, the above relationship incorporates into the simulation the effect of ESS on cellular processes that result in the alteration of the pathways governing the transendothelial transport of water and solutes (e.g., intercellular junctions) (3, 49).

LDL flux is defined across the endothelium by applying J_s as the boundary condition for the convection-diffusion equation (*Eq. 6*). We prescribed a solute flux from the lumen to the arterial wall and conversely applied the following boundary conditions at the luminal and intimal side of the endothelium, respectively:

$$-D_l \nabla c_l n + \mathbf{u}_l c_l n = J_s, \quad (10)$$

$$-D_w \nabla c_w n_w + \mathbf{u}_w c_w n_w = J_s. \quad (11)$$

Moreover, J_v was implemented as boundary condition for the Navier-Stokes equations, and we assumed a lumen-to-wall velocity in the normal direction of the endothelial boundary.

Except for the above-mentioned model of constant normal endothelial permeability for modeling LDL transport, we also performed additional simulations after modifying the permeability term of *Eq. 8* and employing a variable permeability boundary condition dependent on the local lumen LDL concentration (c_l). The relationship between permeability and LDL concentration was derived on the basis of experimental data reported by Guretzki et al. (12). Since the values of endothelial permeability observed in the in vitro endothelial cell culture data were many orders higher than the constant apparent permeability ($P_e = 2 \times 10^{-10}$ m/s) used in our simulations, which better represents the normal in vivo endothelial permeability (52), we scaled the experimental data to match the value calculated for an LDL concentration of 1.272×10^{-3} mol/m^3 (i.e., the average normal LDL concentration in humans) to the above-normal value of constant permeability. The experimental values of apparent endothelial permeability in relation to LDL-cholesterol level were also translated into

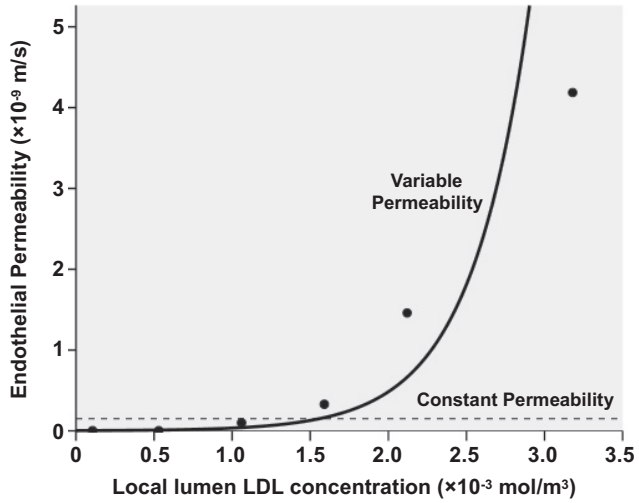

Fig. 4. Relationship between endothelial permeability and lumen-side low-density lipoprotein (LDL) concentration (variable permeability; solid line) derived from in vitro experimental data presented by Guretzki et al. (11). The dotted line denotes the value of constant permeability ($P_0 = 1.5 \times 10^{-10}$ m/s) used in our standard simulations.

diffusive permeability values (using the equations for solute transport included in the APPENDIX) and LDL particle concentration (using the conversion described above), respectively. The curve fitting the values was best described by an exponential relationship between LDL concentration and diffusive permeability (Fig. 4):

$$P_0 = 2.460 \times 10^{-12} e^{2641 c_l} \quad (12)$$

where c_l is the local LDL concentration on the luminal side of the endothelium. In this way, the novel endothelial penetration model depended on ESS as well as on the computed c_l value.

Simulation parameters. Table 1 shows the values of the different parameters used in our study. The Reynolds number and the modified Peclet number (N_{Pe}), defined as the ratio of convective to diffusive fluxes through a single pathway (see APPENDIX for details) (49), were 264 and 0.66 at the site of max stenosis in the stenosed RCA model, respectively. The parameters that varied in our simulations included the intravascular pressure, endothelial permeability, inlet LDL concentration, pulsatile vs. steady flow, and normal heart rate vs. tachycardia.

Regarding the computational mesh of the two arterial geometries, the lumen was discretized into ~1,400,000 hexahedral elements with increased mesh density within the boundary layer of flow near the wall, whereas the arterial wall was discretized into ~3,900,000 elements consisting of bricks and tetrahedrons by using an inflation algorithm; starting from the wall side of the endothelial boundary, 15 layers of brick elements with a maximum thickness of 0.03 mm for each layer were generated, and then the remaining volume in the arterial wall was filled with tetrahedrons. The mesh resolution used in the study was based on a mesh independence analysis, as detailed in the APPENDIX, which demonstrated that the mesh was sufficient for reconstructing the flow field in the lumen and the flow and concentration fields in the arterial wall.

The meshes in the lumen and arterial wall were generated using the commercial software ANSYS Workbench Meshing 12.0 (ANSYS, Canonsburg, PA), and the equations for blood flow and LDL transport modeling were solved iteratively by the finite-volume code in ANSYS CFX 12.0 using an algebraic multigrid approach (15) and pressure-velocity coupling (23). A high-resolution advection scheme (combined second-order central difference with first-order upwind) was applied for spatial discretization and stabilization (1), and a second-order backward Euler scheme was used for the discretization of the transient term in the case of pulsatile flow.

Statistics. Continuous variables are presented as means ± SD. Average cross-sectional ESS and subendothelial LDL accumulation were computed every 0.5 mm along the upstream, throat, and downstream region of the stenosis. The relative change of a continuous variable (V) at a target condition (V_t; e.g., mean LDL concentration when modeling double endothelial permeability) compared with a reference condition (V_{ref}; e.g., mean LDL concentration when modeling normal endothelial permeability) was defined as $100 \times (V_t - V_{ref})/V_{ref}$. The relationship between two continuous variables was investigated using regression analysis and the coefficient of determination (R^2). P values <0.05 were considered statistically significant. The analysis was performed using the Statistical Package for Social Sciences (SPSS version 17.0; Chicago, IL).

RESULTS

The complex 3D arterial geometry of the RCA, characterized by areas with increased local curvature, determined the ESS distribution that, together with the intraluminal pressure, governed LDL accumulation in the subendothelial wall layer. An inverse relationship was demonstrated between ESS distribution and LDL accumulation (Fig. 5).

ESS distribution and subendothelial LDL accumulation along the curved stenosed segment. The presence of the stenosis with the gradual decrease (upstream region) and increase (downstream region) in lumen area (Fig. 6*A*) critically influenced local ESS and LDL distribution. Variations of average cross-sectional ESS magnitude and LDL accumulation in the axial direction for the stenosed and the nondiseased artery are shown in Fig. 6, *B* and *C*, respectively. At the proximal reference location, ESS values were almost identical in the stenosed and the nondiseased model, but within a short distance of 1–2 mm, ESS values increased in the upstream region of the stenosis, reaching a maximum at the location of the minimum lumen area at the throat of the stenosis. Conversely, LDL accumulation gradually decreased in the upstream region, acquiring the lowest values in the region of minimum lumen area.

ESS values remained high (corresponding to low local LDL values) within the entire throat and exhibited a secondary cross-sectional maximum distally at the exit location

Table 1. *Parameter values used in the study*

Parameter	Value	Ref.
Blood density (ρ)	1,060 kg/m^3	29
Blood viscosity (μ)	0.0035 Pa·s	33
Initial (inlet) LDL lumen concentration* (c_0)	0.742, 1.06, 1.696, 2.12 $\times 10^{-3}$ mol/m^3	
Adventitial LDL concentration (c_{adv})	0.005c_0, 0.015c_0	30
Pressure (p)	70, 120 mmHg	30
Pressure in the arterial wall (p_w)	17.5, 30 mmHg	30
Lumen diffusivity (D_l)	5×10^{-12} m^2/s	29
Wall diffusivity (D_w)	8×10^{-13} m^2/s	29
Darcian permeability (k_w)	1.2×10^{-18} m^2	29
Apparent permeability (P_e)	2, 4×10^{-10} m/s	39, 52
Solute lag coefficient (K_{lag})	0.1486	29
LDL degradation rate (r_w)	1.4×10^{-4} s^{-1}	29
Plasma viscosity (μ_p)	0.001 Pa·s	29
Solvent reflection coefficient (σ_f)	0.997	46

*Four clinically meaningful values of LDL-cholesterol concentration were used and converted into LDL particle concentrations based on average measurements in a large human population [Otvos et al. (31)].

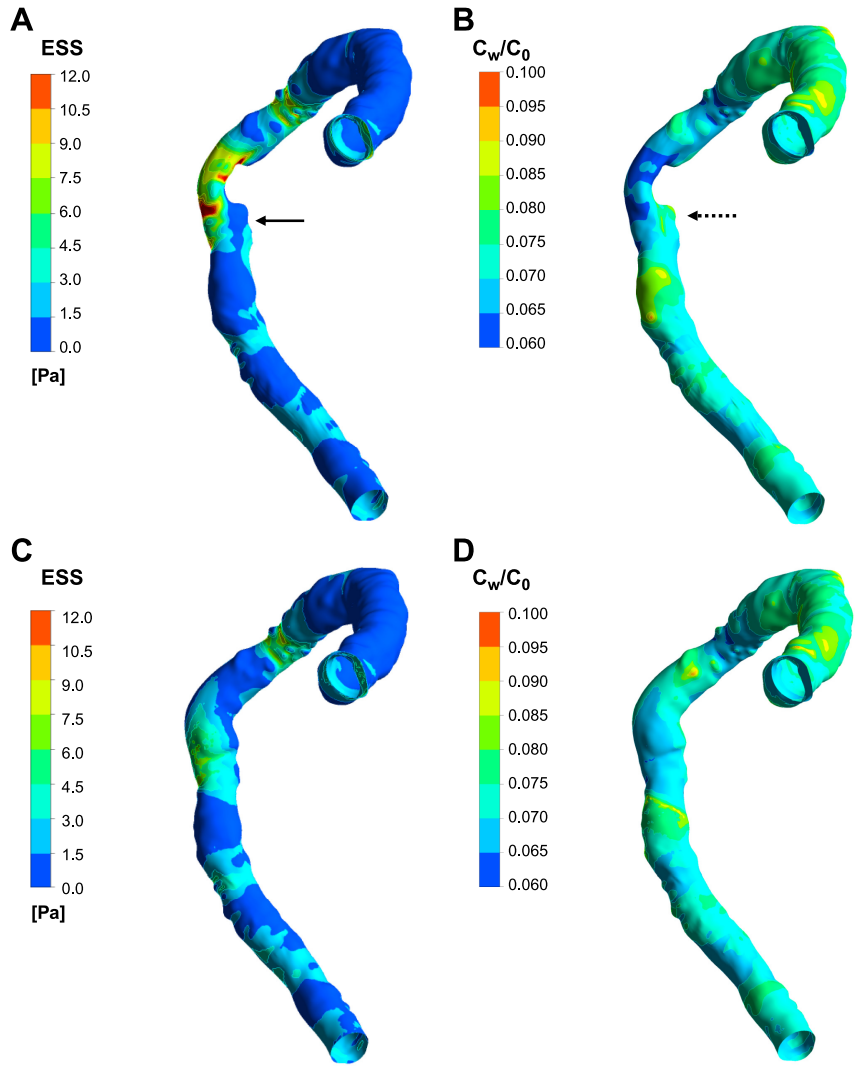

Fig. 5. Endothelial shear stress (ESS) distribution demonstrating high ESS values in the upstream and throat regions of the stenosis (*A*; stenotic model) and lower ESS values in the downstream region, especially on the inner side of the curved segment (arrow). ESS in the respective regions of the nondiseased model (*B*) is quite lower. The corresponding normalized LDL concentration (C_w/C_0) in the subendothelial layer (*C* and *D*) is inversely related to the ESS distribution and exhibits lower values in the throat region of the stenosis and higher values just distal to the stenosis (dotted arrow) in the stenosed model.

of the throat because of the increased arterial curvature and the small lumen size at that location (Figs. 5*A*, 5*C*, and 6). The increased curvature distally at the exit location of the throat skewed blood flow toward the outer side of the curved segment, creating a local ESS increase and, in turn, a decrease in LDL accumulation. The independent effect of arterial curvature was also evident in the nondiseased model with the restored lumen, which had lower ESS values with higher LDL accumulation toward the inner side of the curve compared with the outer side of the arterial segment (Fig. 5, *B* and *D*).

In the downstream region of the stenosis, there was a large area with flow recirculation and low ESS toward the inner side of the curved segment, and this was attributed to the abrupt lumen expansion and the increased local curvature. As shown in Fig. 7, there were two flow recirculation zones, one just downstream of the stenosis and one more distally, which were characterized by low blood flow velocities, leading to increased subendothelial LDL accumulation, presumably because of stagnation of LDL particles that were not "flushed" away by blood flow (i.e., locally increased lumen-side LDL concentration resulting in LDL concentration polarization, which contributed to a relatively increased diffusive component of solute flux; Fig. 7*D*) and thus adhered on the endothelial layer and penetrated into the subendothelial space of the intima. In addition, the ESS-dependent hydraulic conductivity in the present study reflects a direct effect of ESS on the transport properties of the endothelial layer/arterial wall, leading to relatively low transmural velocity in low ESS regions (Fig. 7*E*). However, transmural velocity is a dominant feature of LDL transport in the arterial wall and also leads to the decrease of solute flux by decreasing its convective component (Fig. 7*F*). The end result of reduced J_v is the decrease in the convection of LDL (low efflux) from the subendothelial layer to the outer layers of the arterial wall, leading to the relatively augmented subendothelial LDL accumulation compared with regions with higher ESS and J_v.

Effect of hemodynamic factors: pulsatile blood flow and tachycardia. The time-averaged values of the pulsatile flow simulation in the stenosed model corresponding to the normal heart rate were found to differ from the ones of the respective steady simulation to a variable but small degree depending on

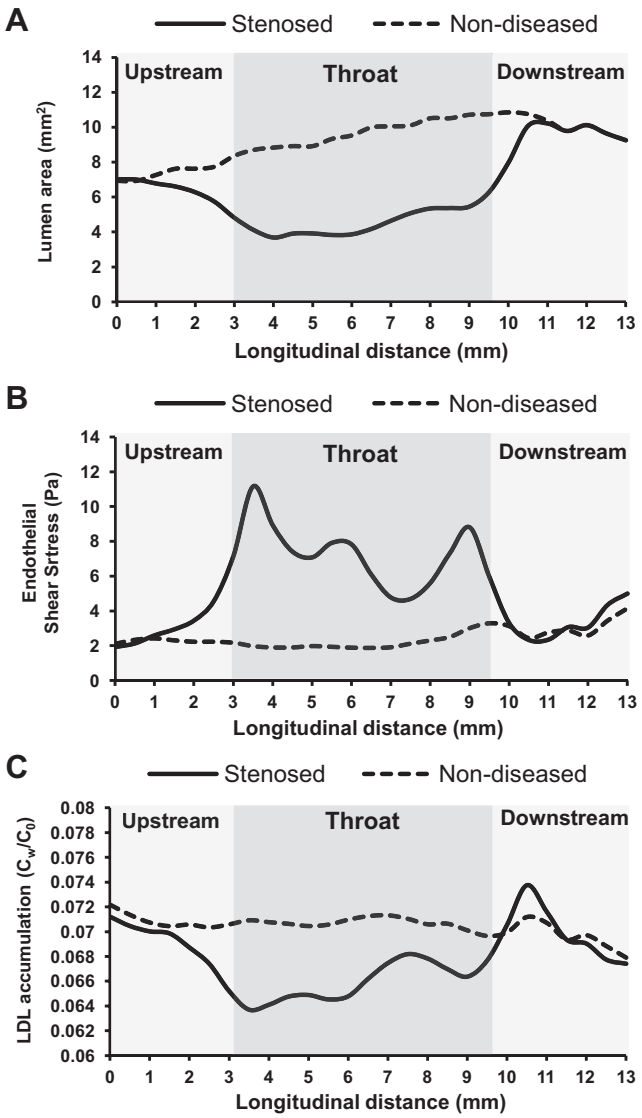

Fig. 6. Profile of lumen area (*A*), average ESS (*B*), and average normalized LDL accumulation (*C*) along the upstream, throat, and downstream regions of the stenotic region in the stenosed and "nondiseased" reconstructed arterial models. In the stenosed model, the gradual decrease of lumen area in the upstream region led to an increase in ESS with a respective decrease in LDL accumulation. The maximum ESS value and the corresponding minimum value of LDL accumulation were observed at the region of minimum lumen area (longitudinal location: 3.5 mm). LDL accumulation remained relatively low throughout the throat of the stenosis and presented a substantial increase in the downstream region colocalizing with sudden lumen expansion and low ESS. In the nondiseased model, ESS and LDL accumulation were relatively uniform with no substantial fluctuations due to the restored arterial lumen.

the location of the stenosed region. ESS values increased in the upstream and throat regions by −1.8% and −3.7%, respectively, whereas there was a decrease of −11.4% in the downstream region. Consequently, there was a prominent increase in LDL accumulation by 3.9% in the downstream region. Tachycardia had a minimal impact on both ESS and LDL accumulation in the three regions of the stenosis model with a decrease of 0.1–0.2% in ESS and an increase of up to 0.2% in time-averaged LDL accumulation during one cardiac cycle, respectively, compared with the normal heart rate profile.

Effect of biological factors: hypertension, LDL serum level, and endothelial permeability. Hypertension was found to play a prominent role in LDL accumulation, leading to augmented local LDL deposition by 55.6% compared with the normotensive case (Fig. 8*A*; Table 2). Similarly, double endothelial permeability also resulted in an increase of 23.5% (Fig. 8*B*; Table 2), whereas the combination of hypertension and double permeability had an additive effect, reaching an increase of 88.6% in local LDL wall concentration (Fig. 8*C*; Table 2).

The subendothelial LDL concentration according to the inlet LDL concentration is depicted in Fig. 9, which shows that there was an overall difference but the relative distribution of LDL accumulation did not change. The lowest local subendothelial concentration was observed for the lowest studied inlet LDL concentration (i.e., 0.742×10^{-3} mol/m^3) with an overall decrease of 56.3% compared with the reference values obtained when the inlet LDL concentration was 1.696×10^{-3} mol/m^3 (Table 2). These changes were similar in the two different lumen geometries (the stenosed and nondiseased model). Conversely, the increased serum level of 2.12×10^{-3} mol/m^3 led to a 25% increase in LDL accumulation along the entire segment in both models. Figure 10 depicts the relationship between the computed mean values of LDL accumulation in the stenotic region (stenosed model) for the four LDL serum levels tested in this study.

The results of the simulations with the proposed model of variable endothelial permeability are presented in Fig. 11 and Table 2. Comparing the overall results with the respective ones of constant normal permeability in all three regions of the stenosed model, we observed substantial differences in LDL accumulation: −24%, −16.7%, 8.6%, and 40.6% for the models with inlet LDL concentration of 0.742, 1.06, 1.696, and 2.12×10^{-3} mol/m^3, respectively. Overall, the effect of increasing values of inlet LDL concentration on LDL accumulation was augmented nonlinearly in this case compared with the model with constant permeability (Fig. 10).

DISCUSSION

Available literature data have primarily described the ESS distribution and its relationship with regions prone to atherosclerosis onset and progression, whereas reports on LDL accumulation in the arterial wall, which constitutes one of the hallmarks of atherosclerosis, especially in patient-specific 3D coronary arterial models, are limited. In the present work, we investigated the influence of a patient-specific 3D complex coronary arterial geometry including a stenosed curved segment on LDL subendothelial accumulation. Moreover, we systematically studied for the first time the effect of several hemodynamic and biological factors on LDL transport modeling and LDL accumulation. Our main observations are as follows. *1*) The curved arterial 3D geometry and the plaque-induced changes in the stenotic region had a great effect on the local subendothelial LDL distribution; LDL accumulation was increased in the inner side of the curved section, and in the presence of a stenosis the LDL regional concentration was considerably increased in the downstream region where flow recirculation zones and low ESS were present, indicating susceptible areas for further plaque growth. *2*) LDL accumulation derived from the pulsatile flow simulation had discernible differences in the downstream region of the stenosed

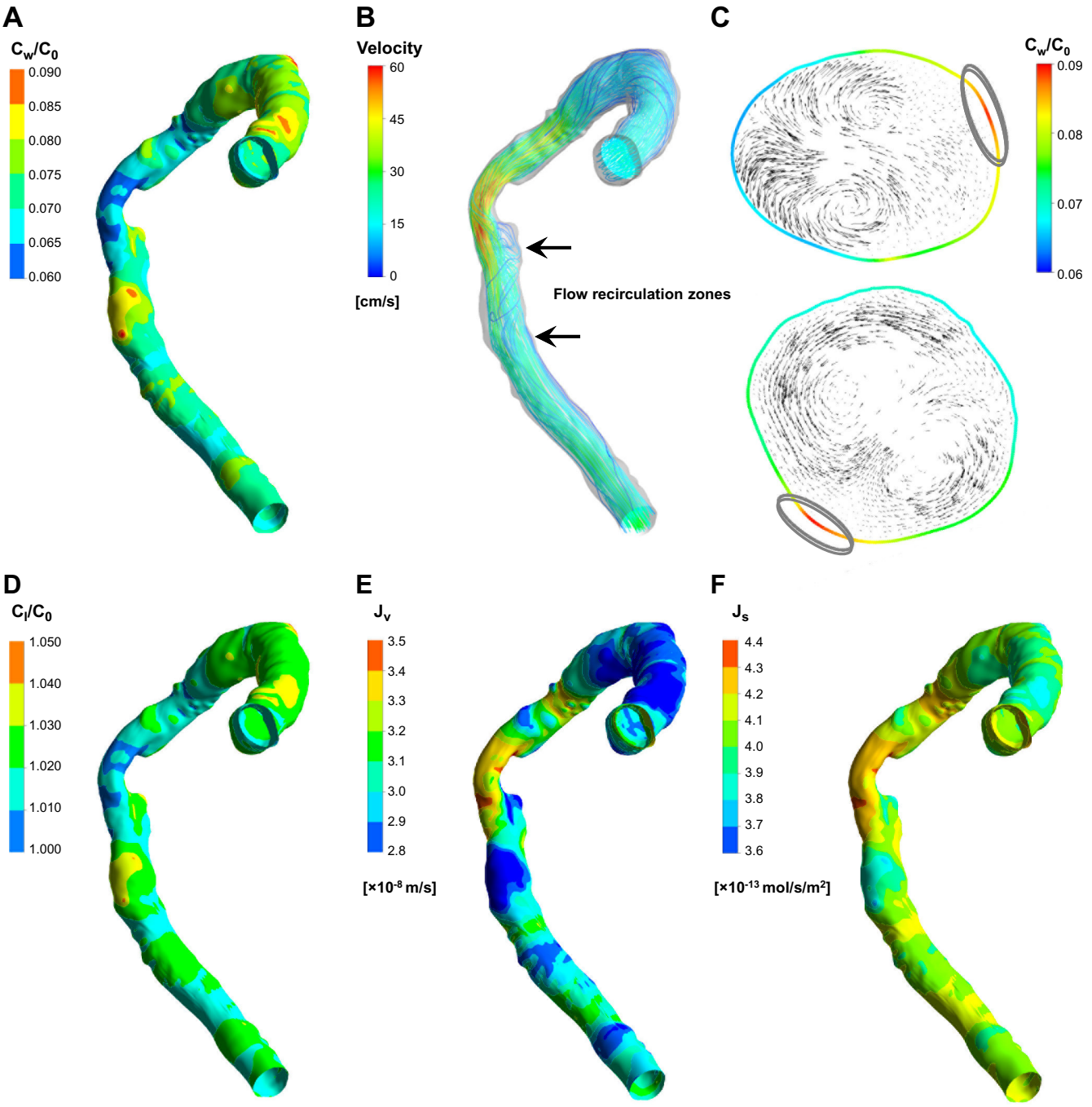

Fig. 7. Colocalization of blood flow recirculation zones with increased LDL accumulation. *A*: normalized LDL accumulation in the subendothelial layer of the arterial wall. *B*: velocity streamlines of blood flow; the arrows indicate 2 regions of disturbed flow and flow recirculation: one just distal to the throat of the stenosis and a second one more distally. *C*: cross-sectional planes (arrows in *B*) at the location of the 2 recirculation zones including secondary velocity vectors and contours of normalized LDL subendothelial accumulation (color scale) indicating increased accumulation (circles) in areas of slow flow. *D*: normalized local lumen-side LDL concentration (C_l/C_0) distribution colocalizes with the subendothelial LDL accumulation. *E* and *F*: the distribution of transmural velocity (J_v) and solute flux (J_s), respectively.

model compared with the steady-state simulation, but the increased heart rate in the RCA had minimal effects in conveying atherosclerotic risk. *3*) Biological risk factors, such as hypertension, endothelial dysfunction resulting in augmented endothelial permeability, and increased LDL serum levels, all greatly influenced the magnitude of LDL accumulation and increased the arterial areas exposed to augmented LDL accumulation, supporting their systemic role in cardiovascular disease.

Effect of arterial stenosis. Arterial stenoses are known to dramatically influence the hemodynamic environment because of lumen compromise. In the current report, the arterial stenosis had a great effect on ESS distribution and the corresponding LDL accumulation, since average ESS was increased by 66 ±

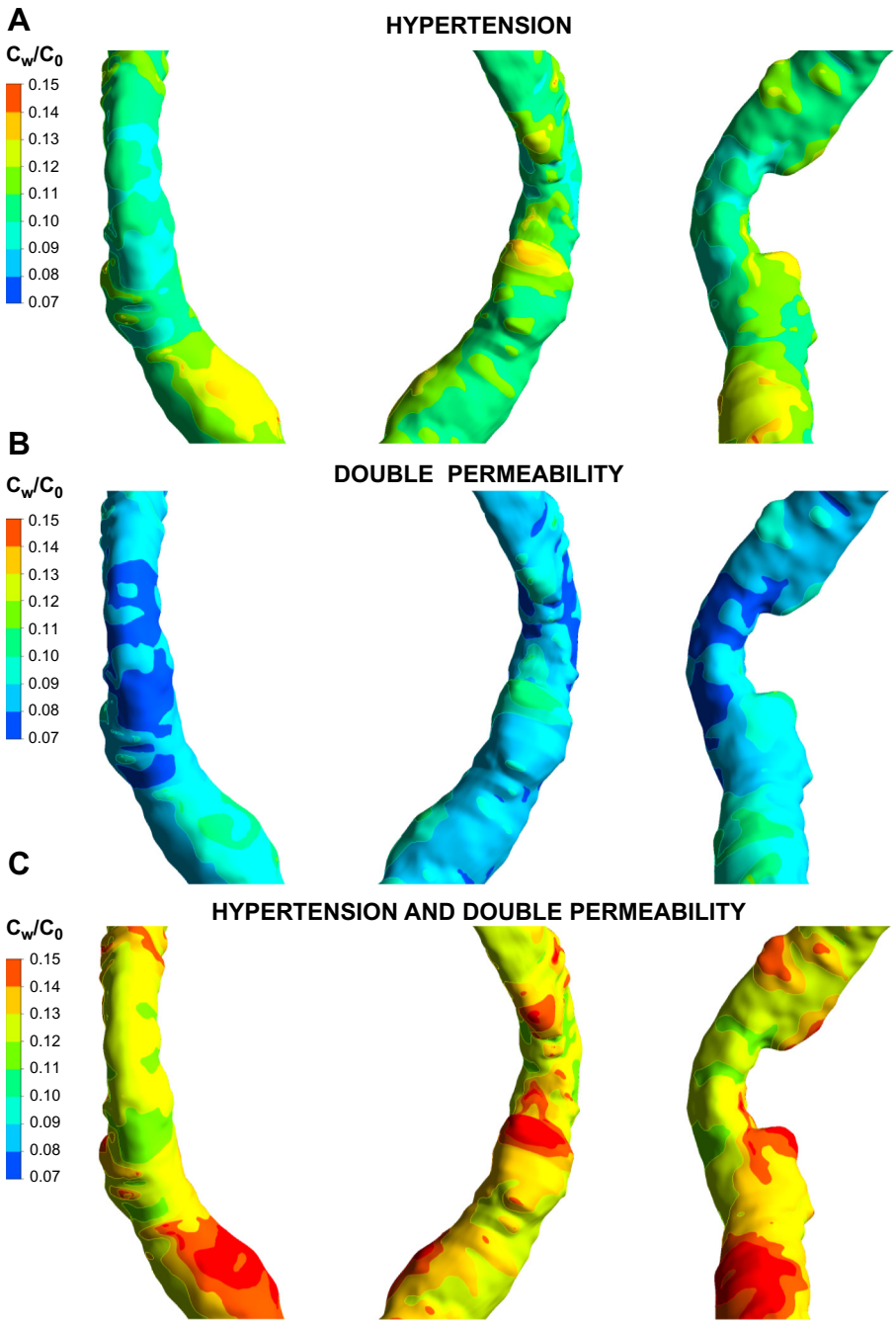

Fig. 8. Normalized subendothelial LDL accumulation in the stenotic region (upstream, throat, and downstream locations) for the cases of hypertension (*A*) and double endothelial permeability (*B*) and the combination of hypertension and double permeability (*C*). Different views are provided: outer side of the curved segment (*left*), inner side (*middle*), and lateral views (*right*).

88%, 240 ± 122%, and 29 ± 17% in the upstream, throat, and downstream regions of the stenosis, respectively, in the stenosed model compared with the nondiseased model. Subsequently, LDL accumulation was reduced by 2.9 ± 2.6% and 6.1 ± 3% in the upstream and throat regions of the stenosed model. In contrast, in the downstream region, flow recirculation zones with slow flow were observed, leading to an increase up to 3.6% (mean: 0.5 ± 2%) in LDL accumulation compared with the nondiseased model (Fig. 7). Furthermore, in the stenosed model, the comparison of the three regions of the stenosis showed that LDL accumulation in the downstream region was considerably increased by 3.4% and 8.6% relative to the upstream and throat regions, respectively (Fig. 6*C*). These results are in agreement with those presented in previous studies (8, 38) showing that plaque growth occurs more frequently in the downstream region of the stenosis rather than the upstream one. This phenomenon should be attributed to the sudden lumen expansion in the downstream region leading to flow separation (47), thereby creating an adverse hemodynamic environment of low ESS. According to our findings and previous studies (46), low ESS contributes to LDL concentration polarization on the luminal side of the endothelium and is also associated with reduced J_v and thus a decrease in the convective clearance of LDL from the subendothelial layer to the outer vessel wall; these low ESS-induced effects synergistically lead to increased subendothelial LDL accumulation and

Table 2. *Effect of various factors on LDL accumulation in the upstream, throat and downstream regions of the stenosis*

Factors		Location Along the Stenotic Region		
		Upstream	Throat	Downstream
Inlet LDL concentration	1.696×10^{-3} mol/m^3 (reference condition)	$C_w = 1.17 \times 10^{-4}$ mol/m^3	$C_w = 1.12 \times 10^{-4}$ mol/m^3	$C_w = 1.21 \times 10^{-4}$ mol/m^3
	0.742×10^{-3} mol/m^3	−56.3%	−56.3%	−56.3%
	1.06×10^{-3} mol/m^3	−37.5%	−37.5%	−37.5%
	2.12×10^{-3} mol/m^3	25%	25%	25%
Hemodynamic	Flow pulsatility	0.4%	−4.2%	3.9%
	Tachycardia	0.2%	0.1%	0.01%
Pressure conditions and pathological endothelial permeability	Hypertension	55.6%	55.6%	55.6%
	Double permeability	23.5%	23.5%	23.5%
	Hypertension and double permeability	88.6%	88.6%	88.6%
Variable permeability and inlet LDL concentration	0.742×10^{-3} mol/m^3	−24%	−24%	−24%
	1.06×10^{-3} mol/m^3	−16.7%	−16.7%	−16.7%
	1.696×10^{-3} mol/m^3	8.6%	8.6%	8.6%
	2.12×10^{-3} mol/m^3	40.6%	40.6%	40.6%

Values are the relative difference (%) in average low-density lipoprotein (LDL) concentration in the subendothelial layer (C_w) of the stenosed arterial model compared with the reference condition (subendothelial LDL concentration derived from the steady flow simulation with 1.696×10^{-3} mol/m^3 inlet LDL concentration assuming steady flow and normal constant endothelial permeability) according to the factors studied and the location at the site of stenosis. Tachycardia (120 beats/min) was compared with the normal heart rate (80 beats/min). The results obtained using variable endothelial permeability with various inlet LDL concentrations are compared with the results for the corresponding concentrations of the reference category.

may explain the results of studies linking low ESS with progressive atherosclerotic disease and a high-risk plaque phenotype (5).

Although the magnitude of the above-mentioned relative increase in LDL accumulation in the downstream region may not seem excessively augmented, it is plausible to argue that the reinforcing nature of the pathobiological processes involved in atherosclerosis may lead from seemingly small differences in LDL particle accumulation to a full-blown inflammatory response with cataclysmic local events. In addition, the resultant absolute differences in LDL accumulation are also dependent on the biological factors (e.g., hypertension and serum LDL level) that contribute to the overall atherosclerotic risk. A relative increase in LDL accumulation may lead to larger differences in absolute values in the presence of other factors that augment the overall LDL accumulation as supported by our results. Therefore, the relative differences in the distribution of LDL accumulation, as those observed along the stenosis, represent the relative difference in potential atherosclerotic development/progression within the context of a given overall/global atherosclerotic risk determined by all contributing factors.

Pulsatile blood flow and high heart rate. Pulsatility is an important feature of blood flow in humans creating oscillations in the flow field with an impact on ESS distribution. Our results showed that there was a discernible decrease in ESS magnitude when the transient simulation was implemented and, of note, that the downstream region of the stenosis was most affected by an average decrease of 11% in ESS. It is plausible that the disturbed and recirculating flow distal to the stenosis was most susceptible to further oscillations caused by flow pulsatility, which lowered the ESS and, consequently, increased the subendothelial LDL accumulation (4% increase).

In patients with coronary artery disease (CAD) a high heart rate may raise myocardial oxygen demand and reduce oxygenation by shortening the diastolic phase, resulting in increased angina symptoms (21). Heidland et al. (14) showed that an increased heart rate is an independent predictor of plaque rupture but failed to identify a direct hemodynamic effect of tachycardia on plaque development and destabilization. In this work we found that tachycardia had overall a small increasing effect on LDL accumulation compared with the normal heart rate. This was due to the fact that in tachycardia the endothelium was exposed for a longer time period to low ESS, because there was a relative increase of the systolic period (i.e., diastolic vs. systolic duration 1:1 in tachycardia vs. 2:1 in the normal heart rate) leading to increase of LDL accumulation (10). The overall accumulated effect over time is evident when we consider that in tachycardia the total time spent on systoles per minute is increased relatively to diastole. However, in the case of RCAs, as in this study, the effect of tachycardia was rather minimal due to high flow in both systole and diastole (Fig. 3). In left coronary arteries, which are characterized by significant differences in flow during the two phases of the cardiac cycle, the effect of tachycardia on LDL accumulation is expected to be more intense and warrants further investigation using transient flow simulations.

Effect of hypertension and augmented endothelial permeability. Hypertension has been recognized as a major risk factor for atherosclerosis because it can cause vessel wall damage, endothelial dysfunction, and intimal thickening. We demonstrated that an elevated blood pressure had a powerful effect on LDL accumulation; an increase of 50 mmHg in blood pressure resulted in a 56% increase in LDL accumulation in all regions. As expected, this increase was similar in the two models (i.e., stenosed and nondiseased) since pressure does not affect the ESS distribution. Pressure-driven convection is one of the main mechanisms that explain the impact of hypertension on transport of macromolecules through the endothelial membrane, and this is directly reflected in our model by increased volume flux. Our results are in agreement with the findings in experimental models that have demonstrated the impact of a raised intraluminal pressure on LDL accumulation and plaque development (7, 9, 25).

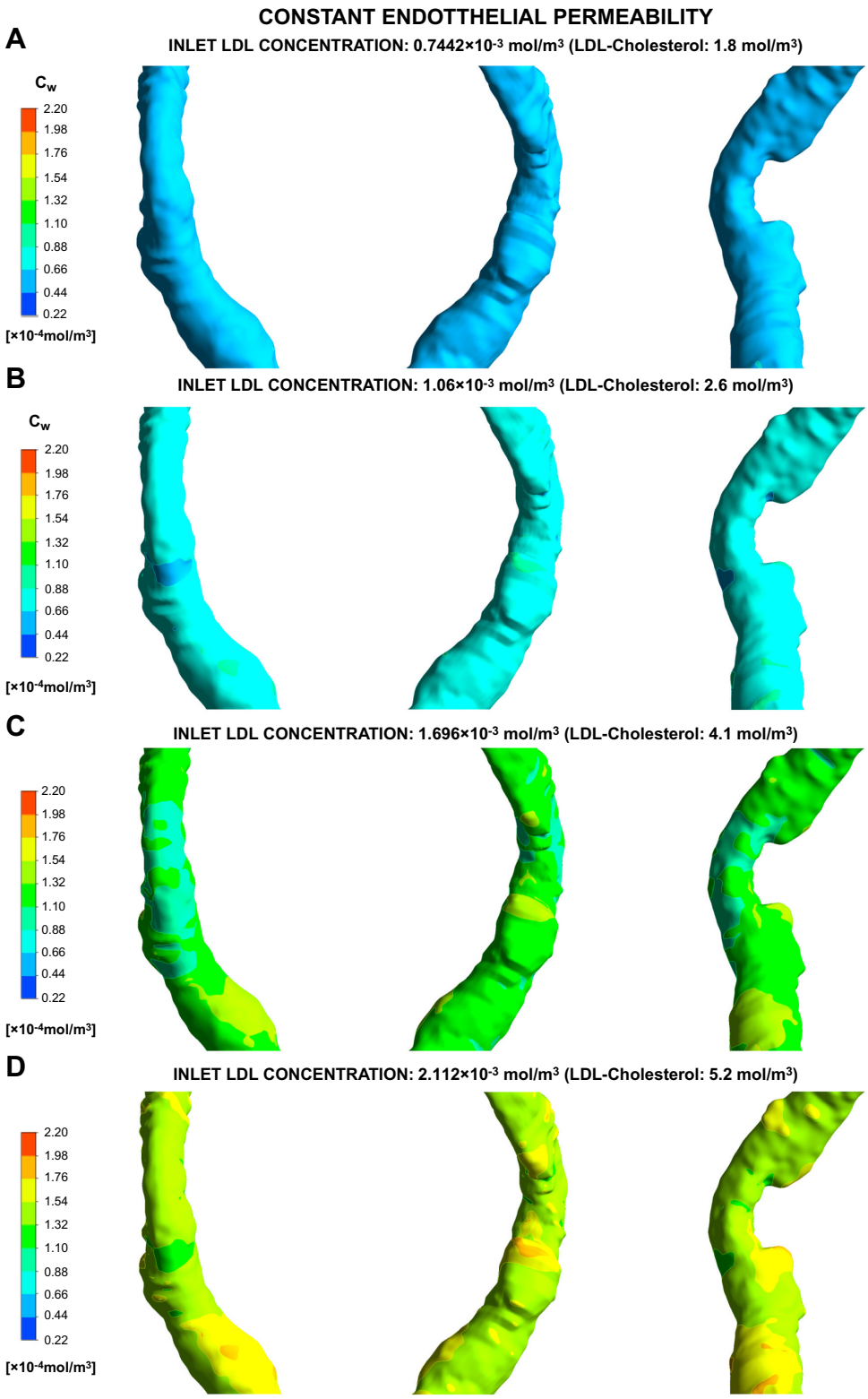

Fig. 9. Subendothelial LDL accumulation (C_w) at the stenotic region (upstream, throat, and downstream locations) with a model of constant endothelial permeability according to 4 different inlet LDL concentrations (serum level): 0.742×10^{-3} mol/m^3 (*A*; corresponding to LDL-cholesterol of 1.8 mol/m^3; ideal target value for patients at very high cardiovascular risk), 1.06×10^{-3} mol/m^3 (*B*; corresponding to LDL-cholesterol of 2.1 mol/m^3; target value for patients at high cardiovascular risk), 1.696×10^{-3} mol/m^3 (*C*; corresponding to LDL-cholesterol of 4.1 mol/m^3; upper normal limit in the general population), and 2.12×10^{-3} mol/m^3 (*D*; corresponding to LDL-cholesterol of 5.2 mol/m^3; increased value above the upper normal limit). Different views are provided: outer side of the curved segment (*left*), inner side (*middle*), and lateral views (*right*).

Another factor that can affect the accumulation of LDL into the arterial wall is a dysfunctional endothelial membrane, as commonly occurs in diabetes mellitus, which may lead to increased permeability of macromolecules (36). We simulated this pathological condition by doubling the value of endothelial permeability, which led to an increase of 23% in LDL subendothelial deposition, demonstrating a direct link between risk factors known to impair endothelial function and LDL infiltration in the arterial wall. As expected, there was an additive effect on LDL accumulation when we combined the hypertensive condition with the raised permeability, resulting in an overall increase of ~90% compared with the normal condition.

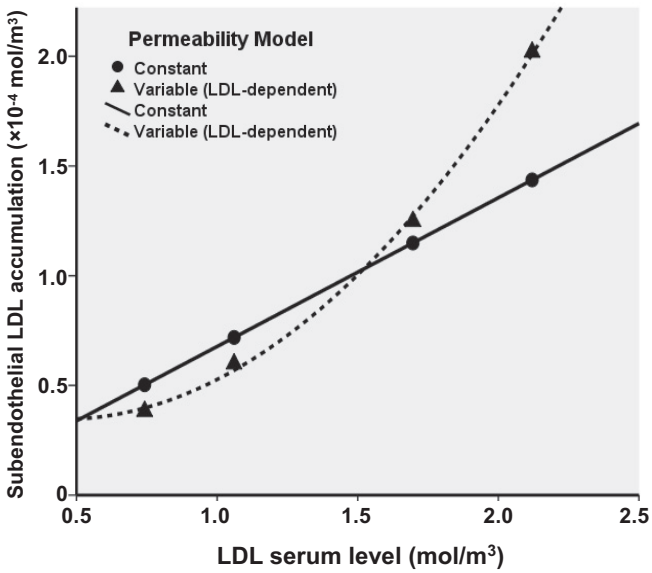

Fig. 10. Relationship between LDL serum level (inlet LDL concentration) and mean computed subendothelial LDL accumulation in the stenotic region (stenosed model) according to the 2 models of endothelial permeability, i.e., constant and variable (LDL dependent). The variable permeability model resulted in augmented LDL accumulation with increasing values of LDL, thereby better reflecting the importance of cholesterol level as a major cardiovascular risk factor.

Except for the above-mentioned effects on the convective component of solute flux, hypertension also causes stretching of the arterial wall that is associated with changes in endothelial cell turnover and abundance of macromolecule micropathways (e.g., leaky junctions) (25, 55), and it is linked to endothelial dysfunction in the clinical setting (50). Therefore, it is likely that the simulation with the combined increase in both parameters reflects more accurately the real conditions in hypertensive patients.

Effect of inlet LDL concentration and LDL-dependent endothelial permeability. Hyperlipidemia is one of the major risk factors of atherosclerosis, and data from large clinical trials have demonstrated that a low LDL serum concentration is associated with better clinical outcomes (27). Our results on LDL accumulation employing the constant endothelial permeability provide further evidence in the same direction showing that there was a mean decrease of ~56% (without affecting the relative LDL distribution) in the stenotic region when the LDL level dropped from 1.696 to 0.742×10^{-3} mol/m^3, which is the ideal target for patients at very high cardiovascular risk. However, it seems that the magnitude of the effect was lower than expected considering the crucial clinical role of reducing hypercholesterolemia.

LDL molecules penetrate the endothelial membrane mainly by leaky junctions and less by LDL receptors (54), and thus LDL penetration is thought to be affected by the LDL concentration on the luminal side of the endothelium. Furthermore, experimental data support the relationship between LDL concentration and endothelial permeability (43), whereas a high-fat diet in swine has been shown to increase the endothelial permeability compared with that in animals fed a normal diet (20). Conversely, small alterations of endothelial permeability have a great effect on LDL endothelial uptake (53, 56). Our results demonstrated a far more enhanced effect of the LDL serum level when the novel model of variable endothelial permeability was applied to LDL mass transport modeling since there was an overall increase of >400% in LDL accumulation when the LDL serum level increased from 0.742 to 2.12×10^{-3} mol/m^3 (Fig. 11), whereas the respective increase was <200% when the constant permeability was used. Therefore, the modeling of a nonconstant but LDL-dependent endothelial permeability may be more appropriate for reflecting the increased atherosclerotic risk with increasing serum LDL levels, especially in the higher range of LDL values.

Potential limitations. This is a proof-of-concept computational study of one patient limited by the availability of imaging data at a single time point, thereby without providing a direct relationship between the local distribution of LDL accumulation and subsequent plaque growth or progression. Pilot animal or patient studies with more than one time point are needed to prove the efficacy of LDL transport modeling in identifying atherosclerosis evolution. In addition, the results regarding the effect of the hemodynamic and biological factors are derived from a single arterial geometry. The extent of the effect is likely to be different in less complex geometries (e.g., straight arterial segments without significant obstruction) or more complex geometries (e.g., coronary bifurcations with obstructive CAD), and thus further research is needed toward this direction to form a more complete view about the impact of these variables on LDL accumulation.

The relationship that we use in this report for defining locally varying permeability on the basis of lumen-side LDL concentration is derived from in vitro endothelial cell cultures, and thus it is not known whether this relationship is valid for in vivo conditions. Since the endothelium has the ability to dynamically adapt to temporal and local requirements, an increased serum LDL level sustained for a long period of time may be adequately compensated by the endothelial cell processes, and as a result, endothelial cell permeability to LDL may not increase as described in the previously published experimental data and the relationship presented in this study. However, in advanced stages of atherosclerosis, passive sieving of LDL across a dysfunctional endothelium with altered transport properties may be facilitated, and thus endothelial permeability may also be dependent on the lumen-side LDL concentration.

The 3D reconstructed model used in the present report is limited by the fact that side branches are not included, an inherent limitation of the reconstruction methodology using angiographic and IVUS data. Nevertheless, the flow disturbances imposed by branching have been shown to diminish within 3 mm (11), and no major branches were present in the stenotic region, which was the region of interest in this study. Finally, we acknowledge that both the motion of the RCA and the vessel compliance were neglected in the current study. However, the RCA motion has been previously shown to have larger effects on the temporal instantaneous ESS measurements, but these effects are much less important on time-averaged ESS values (51, 58). Since the overall accumulated effect of hemodynamics on LDL accumulation over a long time period is more closely represented by time-averaged measurements for attributing local susceptibility for atheroma formation and progression, we do not expect that assuming a stationary (i.e., without motion) RCA had a great effect on our

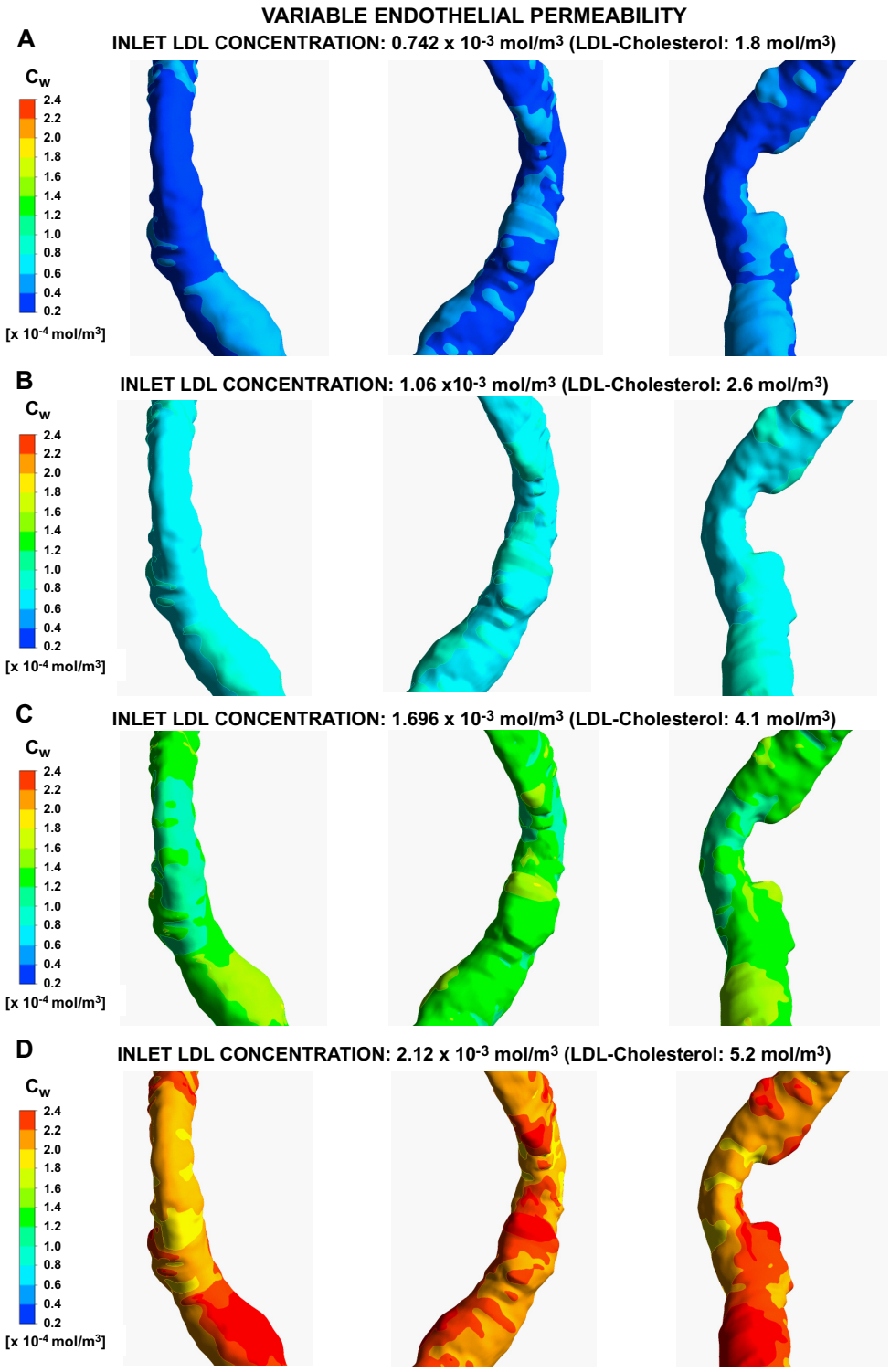

Fig. 11. Subendothelial LDL accumulation at the stenotic region (upstream, throat, and downstream locations) after implementation of the proposed model of variable (LDL dependent) endothelial permeability according to 4 different inlet LDL concentrations (*A–D*; serum level). Different views are provided: outer side of the curved segment (*left*), inner side (*middle*) and lateral views (*right*).

findings. In addition, vessel compliance is not considered to be an important factor influencing local hemodynamics according to previously published reports (57), especially since the stenosis in our study was not in the distal region of the RCA.

Conclusions. In this work, we presented the 3D computational modeling of ESS distribution and LDL subendothelial accumulation in a patient-specific model of a stenosed RCA compared with the same model after the patency of the lumen was restored, thereby showing the great effects of a real stenosis on the local LDL accumulation. Furthermore, we provided for the first time additional evidence and quantified the impact of various hemodynamic and biological factors on LDL deposition supporting the major global role of systemic factors, such as hypertension and LDL serum level, in increasing LDL accumulation. Finally, we showed that modeling of endothelial permeability is critical and that more complex

models of a variable permeability dependent on the local LDL lumen concentration may be necessary to realistically simulate the in vivo pathophysiological processes. This study indicates that computational techniques of LDL transport in the arterial wall can incorporate the factors determining the cardiovascular risk profile of a patient into the modeling process. These complex models are likely to provide a more realistic patient-specific approach in identifying high-risk arterial locations prone to atherosclerosis development.

APPENDIX

Solute transport across the endothelium. Solute transport via diffusion and convection through a single pathway can be described using the following equations (34, 49): $P_e = P_0Z + (J_v)(1 - \sigma_f)$, where σ_f is the reflection coefficient, P_0 is the diffusive permeability, J_v is the transmural velocity, and P_e is the apparent (overall) permeability defined as $P_e = (J_s)/c_l$, where J_s is the solute flux through the endothelium and c_l is the luminal concentration of solute. Z is defined as $Z = N_{Pe}/[\exp(N_{Pe})]$, where N_{Pe} is the Peclet number, $N_{Pe} = [(J_v)(1 - \sigma_f)]$, which indicates the relative importance of convection to diffusion. To calculate P_0 in our model, we first computed the average J_v in the model (model in the reference condition), and then, assuming a literature-based value for P_e, we employed the above-mentioned equations.

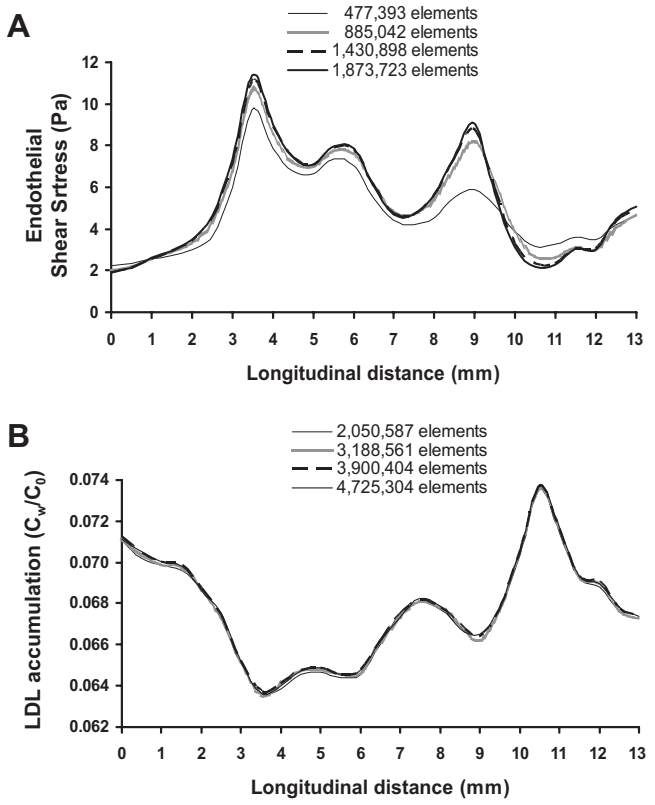

Fig. 12. *A*: average cross-sectional ESS values along the stenotic region (stenosed model) according to mesh resolution (4 different meshes of hexahedrons) in the lumen. The mesh with 1,430,898 hexahedral elements was sufficient for accurate computation of the flow field. *B*: average cross-sectional normalized LDL accumulation (subendothelial space of the arterial wall) along the stenotic region (stenosed model) according to mesh resolution (4 different meshes of brick and tetrahedral elements). The mesh with 3,900,404 elements was sufficient for resolving the concentration field in the wall. The simulations with the different meshes in the wall were performed by using for the lumen the mesh that was previously found to have sufficient resolution.

Mesh independence analysis. Four sets of unstructured meshes, consisting of 477,393, 885,042, 1,430,898, and 1,873,723 hexahedral elements, were generated for the lumen and evaluated to solve the differential equations of fluid motion (Navier-Stokes and continuity) in the arterial lumen of the stenosed model. Comparisons were made between the converged results of each subsequent mesh in the region of stenosis (region of interest in this report) where the flow characteristics were complex and included areas of steep increase and decrease of ESS, as well as flow separation phenomena. Figure 12*A* shows the differences in average cross-sectional ESS magnitude in the solutions obtained with the four meshes along the upstream, throat, and downstream regions of the stenosis. The relative error between the subsequent grids, defined as the difference between the values obtained on the finest mesh and the mesh under consideration relative to the value on the finest mesh, showed that the mesh with 1,430,898 elements provided a sufficient solution for all flow features and ESS computation (relative error margin of 3%).

Four sets of non-uniform unstructured grids, consisting of 2,050,587, 3,188,561, 3,900,404, and 4,725,304 brick and tetrahedral elements, were also evaluated for the computations in the arterial wall, whereas in the lumen the mesh with 1,430,898 hexahedrons, which was previously found to be sufficient, was used. Comparisons between the converged solutions of each subsequent mesh in the wall were again made in the region of stenosis. Figure 12*B* shows the differences in average cross-sectional normalized LDL concentration in the arterial wall (subendothelial layer) along the upstream, throat, and downstream regions of the stenosis. The mesh with 3,900,404 elements was sufficient to accurately calculate the LDL concentration (relative error margin of 0.3% compared with the finest mesh).

GRANTS

This work is partially funded by the European Commission (Project ARTREAT: Multi-level patient-specific artery and atherogenesis model for outcome prediction, decision support treatment, and virtual hand-on training, FP7-224297).

DISCLOSURES

No conflicts of interest, financial or otherwise, are declared by the authors.

AUTHOR CONTRIBUTIONS

A.I.S., M.I.P., and D.I.F. conception and design of research; A.I.S., M.I.P., P.S., L.S.A., T.E., and K.S. analyzed data; A.I.S., M.I.P., C.B., K.K.N., L.K.M., O.P., and D.I.F. interpreted results of experiments; A.I.S. and M.I.P. prepared figures; A.I.S., P.S., L.S.A., T.E., and K.S. drafted manuscript; A.I.S., M.I.P., P.S., L.S.A., T.E., K.S., C.B., K.K.N., L.K.M., O.P., and D.I.F. approved final version of manuscript; M.I.P., C.B., K.K.N., L.K.M., O.P., and D.I.F. edited and revised manuscript.

REFERENCES

1. **Barth TJ, Jesperson DC.** The design and application of upwind schemes on unstructured meshes. AIAA paper 89-0366. In: *AIAA, 27th Aerospace Sciences Meeting, Reno, NV*, 1989.
2. **Bourantas CV, Kalatzis FG, Papafaklis MI, Fotiadis DI, Tweddel AC, Kourtis IC, Katsouras CS, Michalis LK.** ANGIOCARE: an automated system for fast three-dimensional coronary reconstruction by integrating angiographic and intracoronary ultrasound data. *Catheter Cardiovasc Interv* 72: 166–175, 2008.
3. **Chang YS, Yaccino JA, Lakshminarayanan S, Frangos JA, Tarbell JM.** Shear-induced increase in hydraulic conductivity in endothelial cells is mediated by a nitric oxide-dependent mechanism. *Arterioscler Thromb Vasc Biol* 20: 35–42, 2000.
5. **Chatzizisis YS, Baker AB, Sukhova GK, Koskinas KC, Papafaklis MI, Beigel R, Jonas M, Coskun AU, Stone BV, Maynard C, Shi GP, Libby P, Feldman CL, Edelman ER, Stone PH.** Augmented expression and activity of extracellular matrix-degrading enzymes in regions of low endothelial shear stress colocalize with coronary atheromata with thin fibrous caps in pigs. *Circulation* 123: 621–630, 2011.
6. **Cheng C, Tempel D, van Haperen R, van der Baan A, Grosveld F, Daemen MJ, Krams R, de Crom R.** Atherosclerotic lesion size and

vulnerability are determined by patterns of fluid shear stress. *Circulation* 113: 2744–2753, 2006.
7. **Deng X, Marois Y, How T, Merhi Y, King M, Guidoin R, Karino T.** Luminal surface concentration of lipoprotein (LDL) and its effect on the wall uptake of cholesterol by canine carotid arteries. *J Vasc Surg* 21: 135–145, 1995.
8. **Deng X, Marois Y, King MW, Guidoin R.** Uptake of ^{3}H-7-cholesterol along the arterial wall at an area of stenosis. *ASAIO J* 40: 186–191, 1994.
9. **Fry DL, Haupt MW, Pap JM.** Effect of endothelial integrity, transmural pressure, and time on the intimal-medial uptake of serum ^{125}I-albumin and ^{125}I-LDL in an in vitro porcine arterial organ-support system. *Arterioscler Thromb* 12: 1313–1328, 1992.
10. **Giannoglou GD, Chatzizisis YS, Zamboulis C, Parcharidis GE, Mikhailidis DP, Louridas GE.** Elevated heart rate and atherosclerosis: an overview of the pathogenetic mechanisms. *Int J Cardiol* 126: 302–312, 2008.
11. **Gijsen FJ, Wentzel JJ, Thury A, Lamers B, Schuurbiers JC, Serruys PW, van der Steen AF.** A new imaging technique to study 3-D plaque and shear stress distribution in human coronary artery bifurcations in vivo. *J Biomech* 40: 2349–2357, 2007.
12. **Guretzki HJ, Gerbitz KD, Olgemoller B, Schleicher E.** Atherogenic levels of low density lipoprotein alter the permeability and composition of the endothelial barrier. *Atherosclerosis* 107: 15–24, 1994.
13. **Hadjiloizou N, Davies JE, Malik IS, Aguado-Sierra J, Willson K, Foale RA, Parker KH, Hughes AD, Francis DP, Mayet J.** Differences in cardiac microcirculatory wave patterns between the proximal left mainstem and proximal right coronary artery. *Am J Physiol Heart Circ Physiol* 295: H1198–H1205, 2008.
14. **Heidland UE, Strauer BE.** Left ventricular muscle mass and elevated heart rate are associated with coronary plaque disruption. *Circulation* 104: 1477–1482, 2001.
15. **Hutchinson BR, Raithby GD.** A multigrid method based on the additive correction strategy. *Numer Heat Transfer* 9: 511–537, 1986.
16. **Kaazempur-Mofrad MR, Ethier CR.** Mass transport in an anatomically realistic human right coronary artery. *Ann Biomed Eng* 29: 121–127, 2001.
17. **Kaazempur-Mofrad MR, Wada S, Myers JG, Ethier CR.** Mass transport and fluid flow in stenotic arteries: axisymmetric and asymmetric models. *Int J Heat Mass Transfer* 48: 4510–4517, 2005.
18. **Kedem O, Katchalsky A.** Thermodynamic analysis of the permeability of biological membranes to non-electrolytes. *Biochim Biophys Acta* 27: 229–246, 1958.
19. **Koskinas KC, Chatzizisis YS, Baker AB, Edelman ER, Stone PH, Feldman CL.** The role of low endothelial shear stress in the conversion of atherosclerotic lesions from stable to unstable plaque. *Curr Opin Cardiol* 24: 580–590, 2009.
20. **Lamack JA, Himburg HA, Friedman MH.** Effect of hypercholesterolemia on transendothelial EBD-albumin permeability and lipid accumulation in porcine iliac arteries. *Atherosclerosis* 184: 255–263, 2006.
21. **Lang CC, Gupta S, Kalra P, Keavney B, Menown I, Morley C, Padmanabhan S.** Elevated heart rate and cardiovascular outcomes in patients with coronary artery disease: clinical evidence and pathophysiological mechanisms. *Atherosclerosis* 212: 1–8, 2010.
22. **Liu X, Fan Y, Deng X, Zhan F.** Effect of non-Newtonian and pulsatile blood flow on mass transport in the human aorta. *J Biomech* 44: 1123–1131, 2011.
23. **Majumdar S.** Role of underrelaxation in momentum interpolation for calculation of flow with nonstaggered grids. *Numer Heat Transfer* 13: 125–132, 1988.
24. **Malek AM, Alper SL, Izumo S.** Hemodynamic shear stress and its role in atherosclerosis. *JAMA* 282: 2035–2042, 1999.
25. **Meyer G, Merval R, Tedgui A.** Effects of pressure-induced stretch and convection on low-density lipoprotein and albumin uptake in the rabbit aortic wall. *Circ Res* 79: 532–540, 1996.
26. **Moore JA, Rutt BK, Karlik SJ, Yin K, Ethier CR.** Computational blood flow modeling based on in vivo measurements. *Ann Biomed Eng* 27: 627–640, 1999.
27. **Nissen SE, Nicholls SJ, Sipahi I, Libby P, Raichlen JS, Ballantyne CM, Davignon J, Erbel R, Fruchart JC, Tardif JC, Schoenhagen P, Crowe T, Cain V, Wolski K, Goormastic M, Tuzcu EM.** Effect of very high-intensity statin therapy on regression of coronary atherosclerosis: the ASTEROID trial. *JAMA* 295: 1556–1565, 2006.
28. **Olgac U, Knight J, Poulikakos D, Saur SC, Alkadhi H, Desbiolles LM, Cattin PC, Kurtcuoglu V.** Computed high concentrations of low-density lipoprotein correlate with plaque locations in human coronary arteries. *J Biomech* 44: 2466–2471, 2011.
29. **Olgac U, Kurtcuoglu V, Poulikakos D.** Computational modeling of coupled blood-wall mass transport of LDL: effects of local wall shear stress. *Am J Physiol Heart Circ Physiol* 294: H909–H919, 2008.
30. **Olgac U, Poulikakos D, Saur SC, Alkadhi H, Kurtcuoglu V.** Patient-specific three-dimensional simulation of LDL accumulation in a human left coronary artery in its healthy and atherosclerotic states. *Am J Physiol Heart Circ Physiol* 296: H1969–H1982, 2009.
31. **Otvos JD, Mora S, Shalaurova I, Greenland P, Mackey RH, Goff DC Jr.** Clinical implications of discordance between low-density lipoprotein cholesterol and particle number. *J Clin Lipidol* 5: 105–113, 2011.
32. **Papafaklis MI, Bourantas CV, Theodorakis PE, Katsouras CS, Fotiadis DI, Michalis LK.** Association of endothelial shear stress with plaque thickness in a real three-dimensional left main coronary artery bifurcation model. *Int J Cardiol* 115: 276–278, 2007.
33. **Papafaklis MI, Bourantas CV, Theodorakis PE, Katsouras CS, Fotiadis DI, Michalis LK.** Relationship of shear stress with in-stent restenosis: bare metal stenting and the effect of brachytherapy. *Int J Cardiol* 134: 25–32, 2009.
34. **Patlak CS, Goldstein DA, Hoffman JF.** The flow of solute and solvent across a two-membrane system. *J Theor Biol* 5: 426–442, 1963.
35. **Prosi M, Zunino P, Perktold K, Quarteroni A.** Mathematical and numerical models for transfer of low-density lipoproteins through the arterial walls: a new methodology for the model set up with applications to the study of disturbed lumenal flow. *J Biomech* 38: 903–917, 2005.
36. **Schalkwijk CG, Stehouwer CD.** Vascular complications in diabetes mellitus: the role of endothelial dysfunction. *Clin Sci (Lond)* 109: 143–159, 2005.
37. **Sill HW, Chang YS, Artman JR, Frangos JA, Hollis TM, Tarbell JM.** Shear stress increases hydraulic conductivity of cultured endothelial monolayers. *Am J Physiol Heart Circ Physiol* 268: H535–H543, 1995.
38. **Smedby O.** Do plaques grow upstream or downstream?: an angiographic study in the femoral artery. *Arterioscler Thromb Vasc Biol* 17: 912–918, 1997.
39. **Stangeby DK, Ethier CR.** Coupled computational analysis of arterial LDL transport–effects of hypertension. *Comput Methods Biomech Biomed Engin* 5: 233–241, 2002.
40. **Stary HC.** Natural history and histological classification of atherosclerotic lesions: an update. *Arterioscler Thromb Vasc Biol* 20: 1177–1178, 2000.
41. **Stary HC, Chandler AB, Glagov S, Guyton JR, Insull W Jr, Rosenfeld ME, Schaffer SA, Schwartz CJ, Wagner WD, Wissler RW.** A definition of initial, fatty streak, and intermediate lesions of atherosclerosis. A report from the Committee on Vascular Lesions of the Council on Arteriosclerosis, American Heart Association. *Circulation* 89: 2462–2478, 1994.
42. **Steinman DA.** Image-based computational fluid dynamics modeling in realistic arterial geometries. *Ann Biomed Eng* 30: 483–497, 2002.
43. **Stemerman MB, Morrel EM, Burke KR, Colton CK, Smith KA, Lees RS.** Local variation in arterial wall permeability to low density lipoprotein in normal rabbit aorta. *Arteriosclerosis* 6: 64–69, 1986.
44. **Stone PH, Coskun AU, Kinlay S, Clark ME, Sonka M, Wahle A, Ilegbusi OJ, Yeghiazarians Y, Popma JJ, Orav J, Kuntz RE, Feldman CL.** Effect of endothelial shear stress on the progression of coronary artery disease, vascular remodeling, and in-stent restenosis in humans: in vivo 6-month follow-up study. *Circulation* 108: 438–444, 2003.
45. **Sun N, Torii R, Wood NB, Hughes AD, Thom SA, Xu XY.** Computational modeling of LDL and albumin transport in an in vivo CT image-based human right coronary artery. *J Biomech Eng* 131: 021003–021003, 2009.
46. **Sun N, Wood NB, Hughes AD, Thom SA, Xu XY.** Effects of transmural pressure and wall shear stress on LDL accumulation in the arterial wall: a numerical study using a multilayered model. *Am J Physiol Heart Circ Physiol* 292: H3148–H3157, 2007.
47. **Sun N, Wood NB, Hughes AD, Thom SA, Xu XY.** Fluid-wall modelling of mass transfer in an axisymmetric stenosis: effects of shear-dependent transport properties. *Ann Biomed Eng* 34: 1119–1128, 2006.
48. **Sun N, Wood NB, Hughes AD, Thom SA, Yun Xu X.** Influence of pulsatile flow on LDL transport in the arterial wall. *Ann Biomed Eng* 35: 1782–1790, 2007.

49. **Tarbell JM.** Shear stress and the endothelial transport barrier. *Cardiovasc Res* 87: 320–330, 2010.
50. **Thuillez C, Richard V.** Targeting endothelial dysfunction in hypertensive subjects. *J Hum Hypertens* 19, *Suppl* 1: S21–S25, 2005.
51. **Torii R, Keegan J, Wood NB, Dowsey AW, Hughes AD, Yang GZ, Firmin DN, Thom SA, Xu XY.** MR image-based geometric and hemodynamic investigation of the right coronary artery with dynamic vessel motion. *Ann Biomed Eng* 38: 2606–2620, 2010.
52. **Truskey GA, Roberts WL, Herrmann RA, Malinauskas RA.** Measurement of endothelial permeability to ^{125}I-low density lipoproteins in rabbit arteries by use of en face preparations. *Circ Res* 71: 883–897, 1992.
53. **Weinbaum S, Tzeghai G, Ganatos P, Pfeffer R, Chien S.** Effect of cell turnover and leaky junctions on arterial macromolecular transport. *Am J Physiol Heart Circ Physiol* 248: H945–H960, 1985.
54. **Wiklund O, Carew TE, Steinberg D.** Role of the low density lipoprotein receptor in penetration of low density lipoprotein into rabbit aortic wall. *Arteriosclerosis* 5: 135–141, 1985.
54a. **World Health Organization.** *Cardiovascular Diseases*. Geneva: World Health Organization, 2009.
55. **Wu CH, Chi JC, Jerng JS, Lin SJ, Jan KM, Wang DL, Chien S.** Transendothelial macromolecular transport in the aorta of spontaneously hypertensive rats. *Hypertension* 16: 154–161, 1990.
56. **Yuan F, Chien S, Weinbaum S.** A new view of convective-diffusive transport processes in the arterial intima. *J Biomech Eng* 113: 314–329, 1991.
57. **Zeng D, Boutsianis E, Ammann M, Boomsma K, Wildermuth S, Poulikakos D.** A study on the compliance of a right coronary artery and its impact on wall shear stress. *J Biomech Eng* 130: 041014, 2008.
58. **Zeng D, Ding Z, Friedman MH, Ethier CR.** Effects of cardiac motion on right coronary artery hemodynamics. *Ann Biomed Eng* 31: 420–429, 2003.